

Thermodynamic Properties of $^{56,57}\text{Fe}$

E. Algin,¹ U. Agvaanluvsan,² M. Guttormsen,³ A.C. Larsen,³
G.E. Mitchell,^{4,5} J. Rekstad,³ A. Schiller,⁶ S. Siem,³ and A. Voinov⁶

¹*Department of Physics, Eskisehir Osmangazi University, Meselik, 26480 Turkey*

²*Lawrence Livermore National Laboratory, Livermore, CA 94551, USA*

³*Department of Physics, University of Oslo, N-0316 Oslo, Norway*

⁴*North Carolina State University, Raleigh, NC 27695, USA*

⁵*Triangle Universities Nuclear Laboratory, Durham, NC 27708, USA*

⁶*Department of Physics and Astronomy,
Ohio University, Athens, OH 45701, USA*

Abstract

Nuclear level densities for $^{56,57}\text{Fe}$ have been extracted from the primary γ -ray spectra using $(^3\text{He}, ^3\text{He}'\gamma)$ and $(^3\text{He}, \alpha\gamma)$ reactions. Nuclear thermodynamic properties for ^{56}Fe and ^{57}Fe are investigated using the experimental level densities. These properties include entropy, Helmholtz free energy, caloric curves, chemical potential, and heat capacity. In particular, the breaking of Cooper pairs and single-quasiparticle entropy are discussed and shown to be important concepts for describing nuclear level density. Microscopic model calculations are performed for level densities of $^{56,57}\text{Fe}$. The experimental and calculated level densities are compared. The average number of broken Cooper pairs and the parity distribution are extracted as a function of excitation energy for $^{56,57}\text{Fe}$ from the model calculations.

I. INTRODUCTION

Nuclear thermodynamics has attracted considerable attention in recent years. Several temperature-dependent nuclear properties such as nuclear shapes, giant dipole resonance widths and their fluctuation properties have been investigated in the literature [1]. In this context one of the most interesting topics is that of phase transitions in atomic nuclei. Different types of phase transitions have been discussed in nuclear physics. One is the first order phase transition in the multifragmentation of nuclei which occurs at high temperatures [2]. Negative heat capacities observed in multifragmentation of nuclei have been obtained from energy fluctuations and interpreted as an indicator of a first order phase transition [2, 3].

The second type of phase transition in atomic nuclei is the transition from a phase with strong pairing correlations to a phase with weak pairing correlations [4]. The onset of a discontinuity in thermodynamic variables and the evolution of zeros of the canonical [5, 6] and grand-canonical partition functions [6] in the complex plane have been discussed in terms of pairing transitions.

Recently [7], thermal properties for ^{56}Fe have been calculated using both static-path approximation (SPA) and SPA plus random-phase approximation (RPA). These calculations show that the increase of the moment of inertia with increasing temperature is correlated with the suppression of pairing correlations.

Furthermore, structures in the heat-capacity curve related to the quenching of pairing correlations have been obtained within relativistic mean field theory [8], the finite-temperature Hartree-Fock-Bogoliubov theory [9], and the shell-model Monte Carlo (SMMC) approach [10]. An *S*-shaped structure in the heat capacity curve derived from the level densities of low-spin states has also been observed experimentally [11] and interpreted as a signature of a pairing phase transition.

As a part of an ongoing effort, in the present work we extract several thermodynamic properties of ^{56}Fe and ^{57}Fe isotopes starting from nuclear level densities. Details of the experiment, analysis tools, the Oslo method, and experimental level densities are presented in Sect. II. Thermodynamic concepts are discussed in Sect. III and comparison with a combinatorial model is shown in Sect. IV. Finally our results are summarized in Sect. V.

II. EXPERIMENTAL DETAILS AND DATA ANALYSIS

The self-supporting ^{57}Fe target was bombarded by a 2-nA beam of 45-MeV ^3He particles from the Oslo Cyclotron Laboratory at the University of Oslo. The target was isotopically enriched to 94.7%, and had a thickness of 3.4 mg/cm^2 . The outgoing charged particles were recorded by eight Si ΔE -E telescopes, which were collimated and placed 5 cm away from the target at a ring located at 45° with respect to the beam direction. The particle telescopes covered 0.3% of the total solid angle. The thicknesses of the front and the end detectors were 140 and $3000 \text{ }\mu\text{m}$, respectively, and the particle energy resolution was $\approx 0.3 \text{ MeV}$ over the entire spectrum. The reaction γ rays were detected by 28 collimated $5'' \times 5''$ NaI(Tl) detectors with a total efficiency of $\approx 15\%$ of 4π , and with 6% energy resolution at 1.3 MeV. In order to monitor the selectivity and populated spin distribution of the reactions, one 60% Ge(HP) detector was used.

The excitation energy of the final nucleus is determined from the known Q value and the reaction kinematics using particle- γ coincidence information. A total γ -ray spectrum is obtained for each excitation energy region. These γ -ray spectra are then unfolded using a Compton subtraction method [12]. A two-dimensional primary γ -ray matrix is extracted by applying a subtraction method to the unfolded γ -ray spectra [13]. Basic assumptions and details of the subtraction method are given in Ref. [13].

The primary γ -ray matrix is factorized using the Brink-Axel hypothesis [14, 15], according to which the probability of emitting a γ ray from an excited state is proportional to the γ -ray transmission coefficient $\mathcal{T}(E_\gamma)$ and the level density at the final energy $\rho(E - E_\gamma)$. This factorization is determined by a least χ^2 method without assuming any functional form for the level density and the γ -ray transmission coefficient [16]. However, this method does not provide a unique solution. This factorization is invariant under the transformation [16]

$$\begin{aligned}\tilde{\rho}(E - E_\gamma) &= A \exp(\alpha(E - E_\gamma)) \rho(E - E_\gamma) \\ \tilde{\mathcal{T}}(E_\gamma) &= B \exp(\alpha E_\gamma) \mathcal{T}(E_\gamma),\end{aligned}\tag{1}$$

where A , B , and α are the free parameters of the transformation. Therefore it is very important to determine accurately the free parameters A , B , and α in order to find the physical solution. The parameters A and α are determined from the normalization of the

level density to the discrete levels at low excitation energies and to the density of the neutron resonances at the neutron binding energy B_n . The parameter B is then determined using the average total radiative width of neutron resonances [17].

Since there are no neutron resonance data for the ^{56}Fe compound nucleus a different procedure for the normalization of the level density is performed. We use ^{57}Fe as a basis, since both average neutron resonance spacings D and total radiative widths Γ_γ of neutron resonances are well known [18]. The procedure for extracting the total level density $\rho(B_n)$ from the average resonance spacing D is described in Ref. [16]. Then we apply the von Egidy and Bucurescu parameterization of the back-shifted Fermi gas formula [19]

$$\rho_{BSFG} = \eta \frac{\exp(2\sqrt{aU})}{12\sqrt{2}a^{1/4}U^{5/4}\sigma}, \quad (2)$$

where a is the level density parameter, and the intrinsic excitation energy $U = E - E_1$ is determined by the backshift parameter E_1 . In this global description of the level density, shell corrections are taken into account in the estimation of the a and E_1 parameters [19]. By fitting ρ_{BSFG} to $\rho(B_n)$ in ^{57}Fe , we determine the normalization parameter $\eta = 0.852$ of Eq. (2). This value is then adopted for ^{56}Fe together with the prescribed a and E_1 parameters. The parameters used are listed in Table I.

Figure 1 shows the level densities of $^{56,57}\text{Fe}$ from the ground state up to $E \sim B_n - 1$ MeV. They are normalized to discrete levels at low excitation energies (jagged lines) and to the level densities at the neutron binding energy B_n (triangles). The arrows indicate the fitting regions used. As described above, the triangles are determined from Eq. (2) with $\eta = 0.852$ for ^{56}Fe and from the observed D value for ^{57}Fe .

The level density obtained with the Oslo method follows well that obtained by counting of discrete levels up to around 5 and 2.5 MeV of excitation energies in $^{56,57}\text{Fe}$, respectively. Both nuclei show an abrupt increase in level density at $E = 2 - 3$ MeV, indicating the first breaking of nucleon Cooper pairs.

Figure 1 also includes level densities from particle evaporation data (open circles) measured with the $^{55}\text{Mn}(d,n)^{56}\text{Fe}$ reaction [20], and with the $^{58}\text{Fe}(^3\text{He},\alpha)^{57}\text{Fe}$ and $^{59}\text{Co}(d,\alpha)^{57}\text{Fe}$ reactions [21]. The method determines the slope of the level densities, but not the absolute normalization constant. Thus, these data have been scaled to match ρ_{BSFG} (solid smooth curves). The slopes of the level densities from evaporation studies fit very well with the employed ρ_{BSFG} . This gives support to the level density parameters a extracted as prescribed

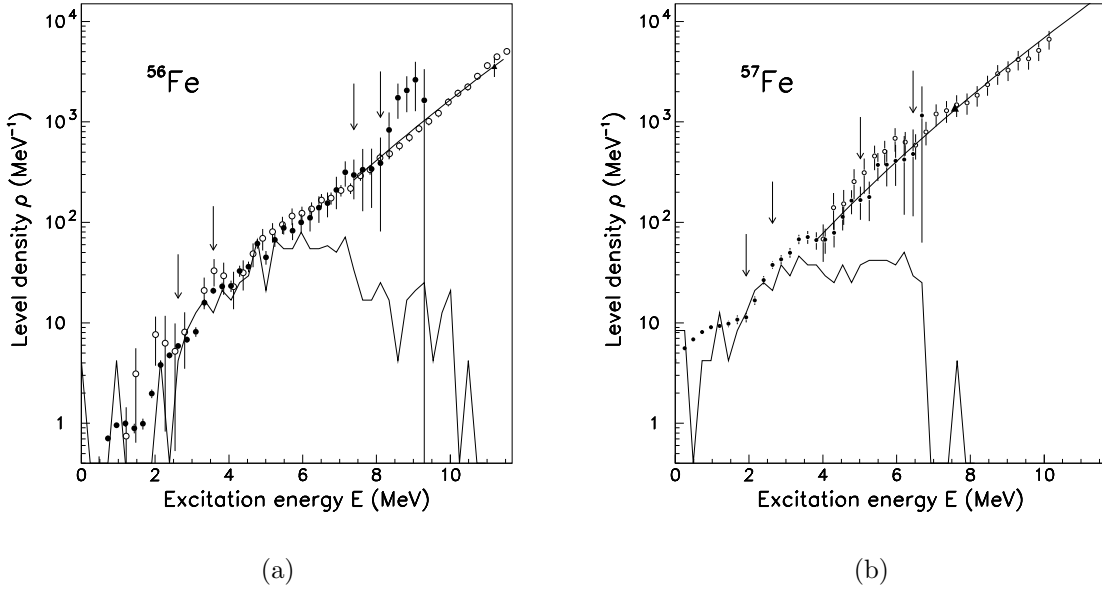


FIG. 1: (a) Experimental level density of ^{56}Fe (full circles). The jagged solid lines represent the level density obtained from counting of discrete levels [23]. The smooth solid curve is the renormalized level density parametrization according to von Egidy and Bucurescu [19]. The data points between the arrows at low and high excitations are used for the normalization. The triangle at B_n is determined from ρ_{BSFG} with $\eta = 0.852$. The level density obtained from the $^{55}\text{Mn}(d,n)^{56}\text{Fe}$ reaction [20] (open circles) is scaled with a factor of 1.3. (b) Experimental level density of ^{57}Fe (full circles). The triangle at B_n is determined from neutron resonance spacings. The level density obtained from the $^{58}\text{Fe}(^3\text{He},\alpha)^{57}\text{Fe}$ reaction [21] (open circles) is scaled with a factor of 2.6.

in Ref. [19] and listed in Table I.

From Eq. (1) we see that the α parameter determines the slope of the transmission coefficient, and thereby also the radiative strength function (RSF) $f(E_\gamma) = \mathcal{T}(E_\gamma)/(2\pi E_\gamma^3)$, assuming only dipole radiation. The RSFs have been published previously [20, 22], but with other normalization procedures. Thus, for completeness, we show in Fig. 2 the renormalized RSFs. In the ^{57}Fe case, the B parameter of Eq. (1) was determined from the average radiative width $\langle\Gamma_\gamma\rangle$ of neutron resonances at B_n [18]. For ^{56}Fe , where no $\langle\Gamma_\gamma\rangle$ exists, we scale the total RSF to match ^{57}Fe . The parameters are listed in Table I.

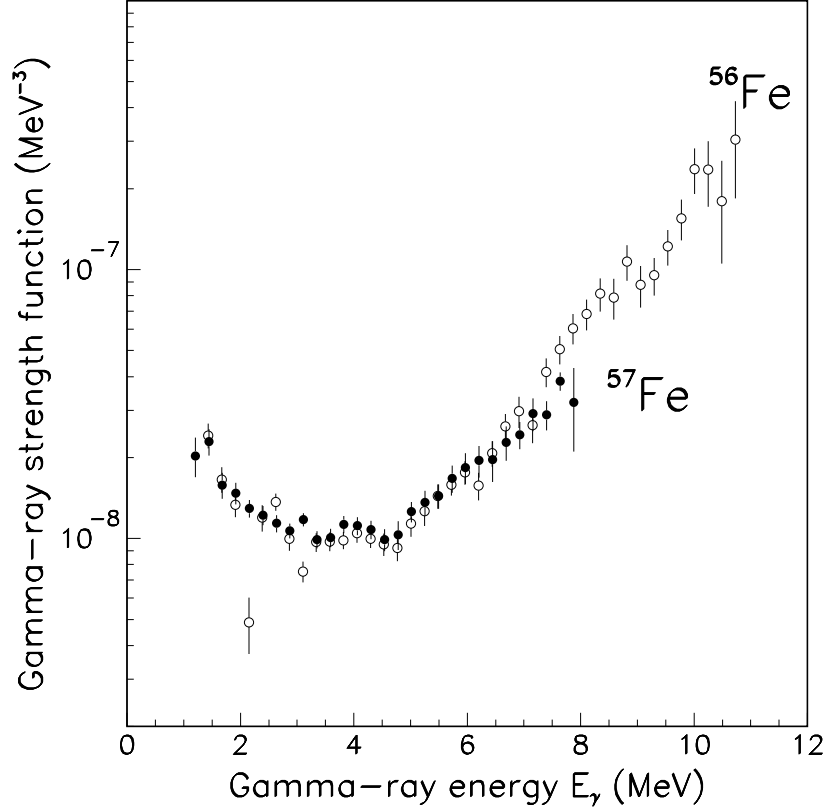


FIG. 2: Radiative strength functions for ^{56}Fe and ^{57}Fe .

TABLE I: Back-shifted Fermi gas level density parameters and normalization constants.

Isotope	B_n	a	E_1	D	$\sigma(B_n)$	η	$\rho(B_n)$	$\langle\Gamma_\gamma\rangle$
	(MeV)	(MeV $^{-1}$)	(MeV)	(keV)			(MeV $^{-1}$)	(meV)
^{56}Fe	11.197	6.196	0.942	2.6(6) ^a	4.049	0.852 ^a	3600(800) ^a	2300(1200) ^a
^{57}Fe	7.646	6.581	-0.523	22.0(17)	3.834	0.852	1380(170)	900(470)

^a Based on systematics, see text.

III. THERMODYNAMIC QUANTITIES

Depending on the system under study, one can chose among different kinds of statistical ensembles in order to derive thermodynamic quantities. The thermodynamic quantities derived within different ensembles give the same results in the thermodynamic limit. On

the other hand, the choice of a specific ensemble may change results significantly for small systems. For example, the caloric curves derived within the microcanonical and canonical ensembles coincide for large systems; but the two caloric curves depart from each other for small systems [24, 25].

The microcanonical ensemble is commonly accepted as the appropriate ensemble to use in investigating atomic nuclei, as the nuclear force has a short range and the nucleus does not share its excitation energy with its surroundings. However some thermodynamic quantities such as temperatures and heat capacities may have large fluctuations and negative values when derived within the microcanonical ensemble. On the other hand, the canonical ensemble averages too much over structural changes of the system. Therefore, it is difficult to choose an appropriate ensemble for a small system. Here, we use both microcanonical and canonical ensembles to study the thermodynamic properties of the system.

A. Microcanonical Ensemble

The microcanonical entropy is closely related to the level density of the system at a given excitation energy. Several thermodynamic properties of the atomic nucleus can be derived from the entropy. The entropy is defined as the natural logarithm of the multiplicity Ω of accessible states within the energy interval E and $E + \delta E$:

$$S(E) = k_B \ln \Omega(E), \quad (3)$$

where k_B is the Boltzmann's constant. Here we set k_B to unity so that the entropy becomes dimensionless and thus the temperature T has the unit of MeV. One should note that the experimental level density is not the true multiplicity of states; i.e., it does not include the $(2I + 1)$ degeneracy of magnetic substates. Thus, in order to obtain the state density Ω , one needs to know the spin distribution as a function of excitation energy. The spin distribution is usually assumed to be Gaussian with a mean of $\langle 2I + 1 \rangle = \sqrt{2\pi}\sigma$, where σ is the spin cut-off parameter which depends very weakly ($\sigma \propto E^{1/4}$) on excitation energy.

However, in this work we define a “pseudo” entropy based on the experimental level density, i.e., $\Omega(E) = \rho(E)/\rho_0$. The normalization constant ρ_0 is introduced and adjusted such that the third law of thermodynamics is fulfilled as $S(T \rightarrow 0) = 0$. The ground states of even-even nuclei represent a well-ordered system with no thermal excitation and

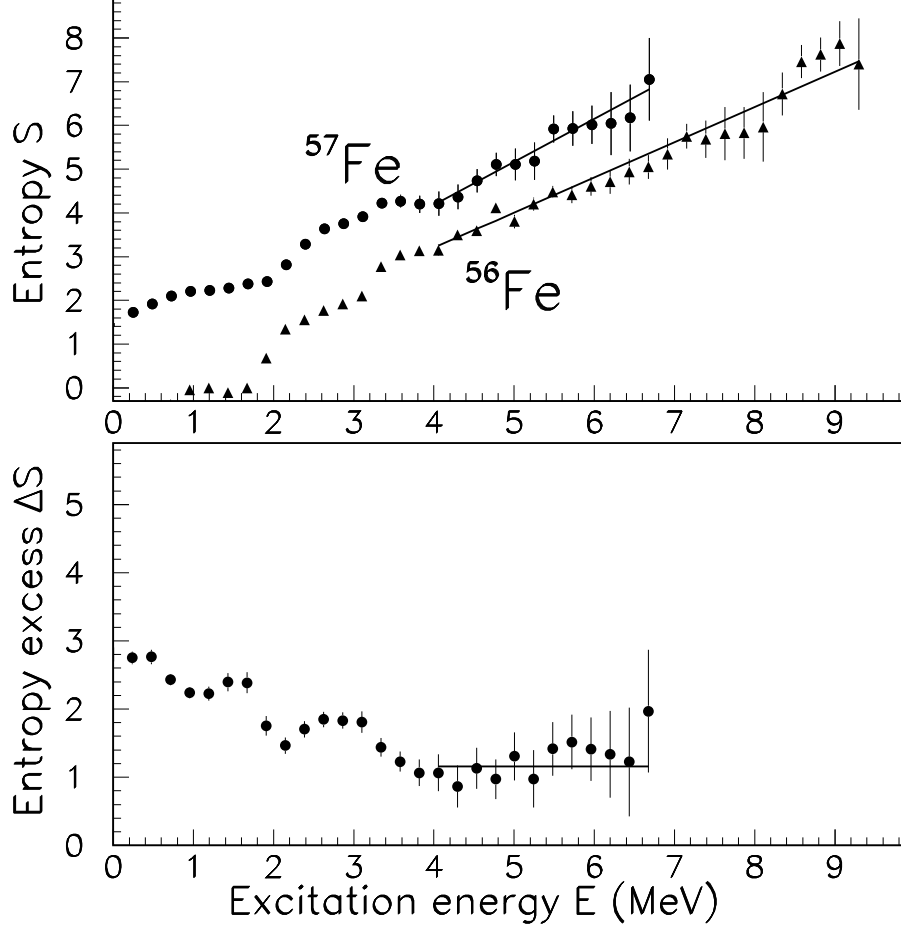


FIG. 3: Upper panel: Deduced entropies for $^{56,57}\text{Fe}$. The solid line is the constant temperature least square fit to the data. Lower panel: Deduced entropy excess for the single particle calculated using Eq. (5). The entropy excess is $\Delta S = 1.2(4)$.

are characterized by zero entropy and temperature. Therefore the normalization constant is set to $\rho_0 = 1 \text{ MeV}^{-1}$ in order to obtain $S = \ln \Omega \sim 0$ in the ground state band region of ^{56}Fe . The extracted ρ_0 is also used for the ^{57}Fe nucleus.

Figure 3 shows the entropies of $^{56,57}\text{Fe}$. The breaking of the first Cooper pair appears in the $E = 2 - 3 \text{ MeV}$ excitation energy region for both nuclei, indicating a slightly delayed breaking for ^{57}Fe due to the odd valence neutron.

The entropies of $^{56,57}\text{Fe}$ appear fairly linear at high excitation energies, and the slope of

the entropy is related to the temperature of the system by

$$T = (dS/dE)_V^{-1}. \quad (4)$$

The entropies of $^{56,57}\text{Fe}$ are fit with a constant temperature model, shown with solid lines in Fig. 3. From this model, constant temperatures of $T = 1.2(3)$ MeV and $T = 1.0(3)$ MeV are found for ^{56}Fe and ^{57}Fe , respectively. These temperatures are interpreted as the critical temperatures T_c for the breaking of nucleon pairs.

The entropy difference between the even-odd and even-even nuclei is interpreted as the entropy of a single quasiparticle (particle or hole), assuming that the entropy is an extensive (additive) quantity. The entropy carried by the valence neutron particle in our case can be estimated by

$$\Delta S = S(^{57}\text{Fe}) - S(^{56}\text{Fe}). \quad (5)$$

The lower panel of Fig. 3 shows the single particle entropy as a function of excitation energy. The fluctuations at the low excitation energies result from the lower pairing gap in the odd-mass system. At higher excitation energies above ~ 4 MeV, the entropy difference has a relatively constant value, revealing the statistical behavior of these isotopes, $\Delta S = 1.2(4)$. This value is less than the value obtained for the rare-earth isotopes which is $\Delta S = 1.7$ [26]. This is expected because ^{56}Fe and ^{57}Fe isotopes are in the vicinity of closed shells, thus the entropy is less than that of the rare-earth isotopes.

Assuming a constant ΔS and a constant energy shift Δ between the two entropies, these two quantities are connected to the critical temperature T_c [26] by

$$T_c = \frac{1}{\Delta S} \Delta. \quad (6)$$

From this relation, we can calculate the entropy difference $\Delta S = \Delta/T_c = 1.5/1.1 \sim 1.4$, which is consistent with the present observations. Here, the gap parameter Δ is assumed to include both the pairing gap and the contribution from the distance between the Fermi surface and the closest neutron orbital.

B. Canonical Ensemble

In a canonical ensemble, a physical system is in thermal equilibrium with a heat reservoir at constant temperature and can exchange energy (but not particles) with the reservoir.

Analogous to the entropy in the microcanonical ensemble, the partition function is the starting point to obtain the thermodynamics of a system in the canonical ensemble. The partition function for a given temperature is determined by

$$Z(T) = \sum_{E=0}^{\infty} \rho(E) \delta E e^{-E/T}, \quad (7)$$

where $\rho(E)$ is the measured level density, and δE is the energy bin used. The summation in $Z(T)$ goes to infinity and our level densities extend to $\sim B_n - 1$ MeV. Therefore we extrapolate the experimental level densities using the BSFG model parameterized by von Egidy and Bucurescu [19]. The Helmholtz free energy can be calculated from the partition function by

$$F(T) = -T \ln Z(T). \quad (8)$$

This equation gives the connection between statistical mechanics and thermodynamics in the canonical ensemble, as does the entropy in the microcanonical ensemble. Then the entropy S , the average excitation energy $\langle E \rangle$, the heat capacity C_V , and the chemical potential μ at a given temperature can be derived from $F(T)$ by

$$S(T) = - \left(\frac{\partial F}{\partial T} \right)_V, \quad (9)$$

$$\langle E(T) \rangle = F + TS, \quad (10)$$

$$C_V(T) = \left(\frac{\partial \langle E \rangle}{\partial T} \right)_V, \quad (11)$$

$$\mu(T) = \frac{\partial F}{\partial n}, \quad (12)$$

where n is the number of thermal particles. These thermal particles outside a core of Cooper pairs are responsible for the thermal properties of the nucleus at low excitations. At higher temperatures, pairing correlations are quenched, and the nucleus has a transition from a paired to unpaired phase.

Figure 4 shows the Helmholtz free energy F , average excitation energy $\langle E(T) \rangle$, entropy S , and heat capacity C_V for ^{56}Fe (dashed lines) and ^{57}Fe (solid lines). The Helmholtz

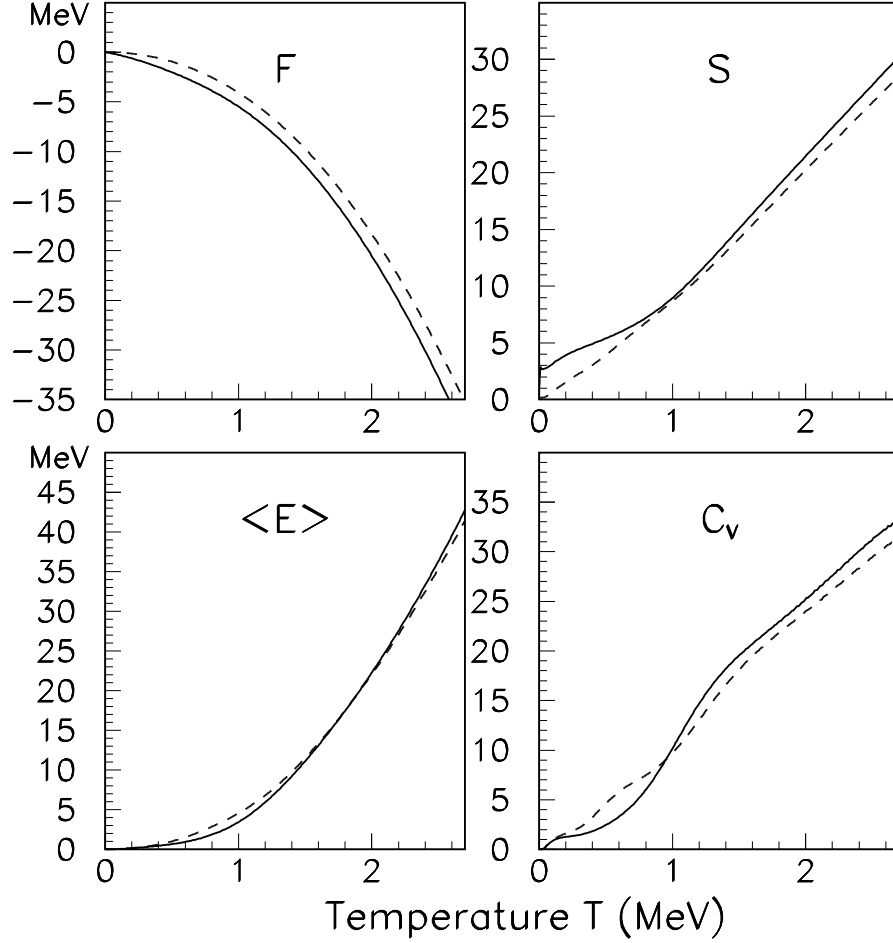


FIG. 4: The Helmholtz free energy F , average excitation energy $\langle E(T) \rangle$, entropy S , and heat capacity C_V for ^{56}Fe (dashed lines) and ^{57}Fe (solid lines), deduced in the canonical ensemble.

free energy F and the average excitation energy $\langle E(T) \rangle$ behave smoothly as a function of temperature. At around $T \sim 1.3$ MeV, both isotopes are excited to energies comparable to their respective neutron binding energies. Average excitation energies for ^{56}Fe and ^{57}Fe coincide only at one point $T \sim 2$ MeV. Above this temperature the odd isotope has larger values as the temperature increases. The entropy S and heat capacity C_V are the first and second derivatives of F , respectively, and thus both reflect thermal variations. For temperatures below $T = 1$ MeV, the entropy difference for ^{56}Fe and ^{57}Fe reaches ~ 2 , the entropy of ^{57}Fe being larger. The entropies have similar values for $T = 1 - 1.5$ MeV. Above $T = 1.5$ MeV, the two entropies start to diverge. Both heat capacities have an S shape

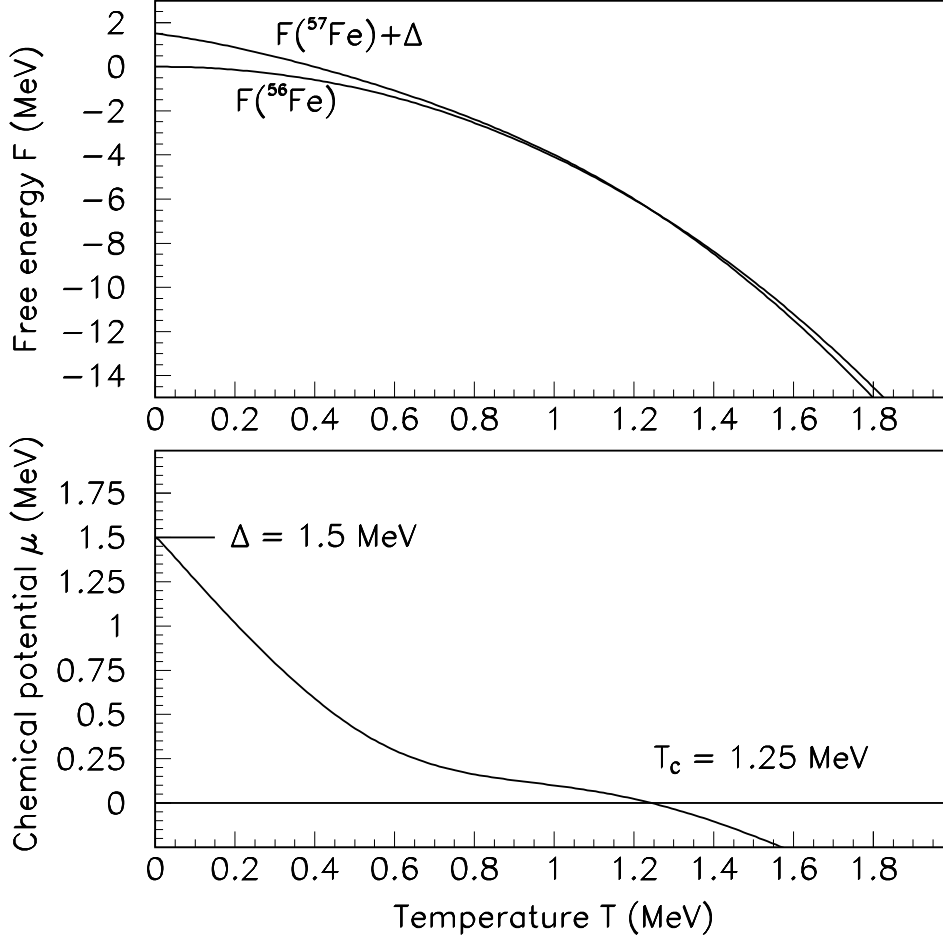


FIG. 5: The experimental Helmholtz free energies deduced in the canonical ensemble for ^{56}Fe and ^{57}Fe . The critical temperature for the quenching of pairing correlations is indicated by T_c , where the chemical potential is $\mu \sim 0$.

which is interpreted as a fingerprint for pairing transitions in nuclei. The structure in the heat capacity C_V for ^{57}Fe is more pronounced than the C_V for ^{56}Fe , which is the opposite of what SMMC calculations predict. The contribution to the heat capacity from collective excitations is negligible, and has no influence on the S shape [27].

Figure 5 shows the chemical potential μ which is defined as the amount of energy required to excite a nucleon from the underlying core of paired nucleons, while the entropy and volume held fixed. The typical energy cost for creating a quasiparticle is $-\Delta$ which is also equal to the chemical potential. The chemical potential can be written as

$$\mu = \frac{\Delta F}{\Delta N} = \frac{F_{odd} - F_{even}}{1} = -\Delta. \quad (13)$$

thus giving $F_{even} = F_{odd} + \Delta$. The energy curve of ^{57}Fe can be interpreted as the free energy for an even-even system with one extra nucleon.

C. Probability Density Functions

An alternative way of studying the energy-temperature relation of a system is the probability density function, which is the probability of the system having energy E for a given temperature, and is given by

$$P(E) = \frac{\Omega(E) \exp(-E/T)}{Z(T)}. \quad (14)$$

In the thermodynamic limit $P(E)$ is very sharp - similar to a δ function. However, for small systems the multiplicity of states is much smaller, which makes the probability distribution broader. Figure 6 shows the probability density functions for $^{56,57}\text{Fe}$ nuclei for various temperatures. Below $T \sim 1$ MeV, the distribution is mainly based on the experimental level density. For increasing temperatures, the energy of the nucleus increases; therefore, the probability density function depends more and more on the extrapolated level density.

Below $T = 1.2$ MeV, the distribution is slightly broader for ^{56}Fe due to collective excitations below the pairing gap in this nucleus. The effect of critical temperatures obtained with the constant temperature least-square fit can also be seen on the probability density function. At $T_c = 1.2$ MeV and $T_c = 1.0$ MeV for $^{56,57}\text{Fe}$, respectively, the probability distribution becomes broader where the breaking of nucleon pair process is strongest.

IV. COMPARISON OF LEVEL DENSITIES WITH MICROSCOPIC CALCULATIONS

In order to extract more information on the underlying nuclear structure resulting in the observed level density, we have performed microscopic calculations with the code MICRO [28]. The code is based on a model employing Bardeen-Cooper-Schrieffer (BCS) quasiparticles [29], which are distributed on all possible proton and neutron configurations according to the given excitation energy E of the nucleus. The advantage of this code is a fast

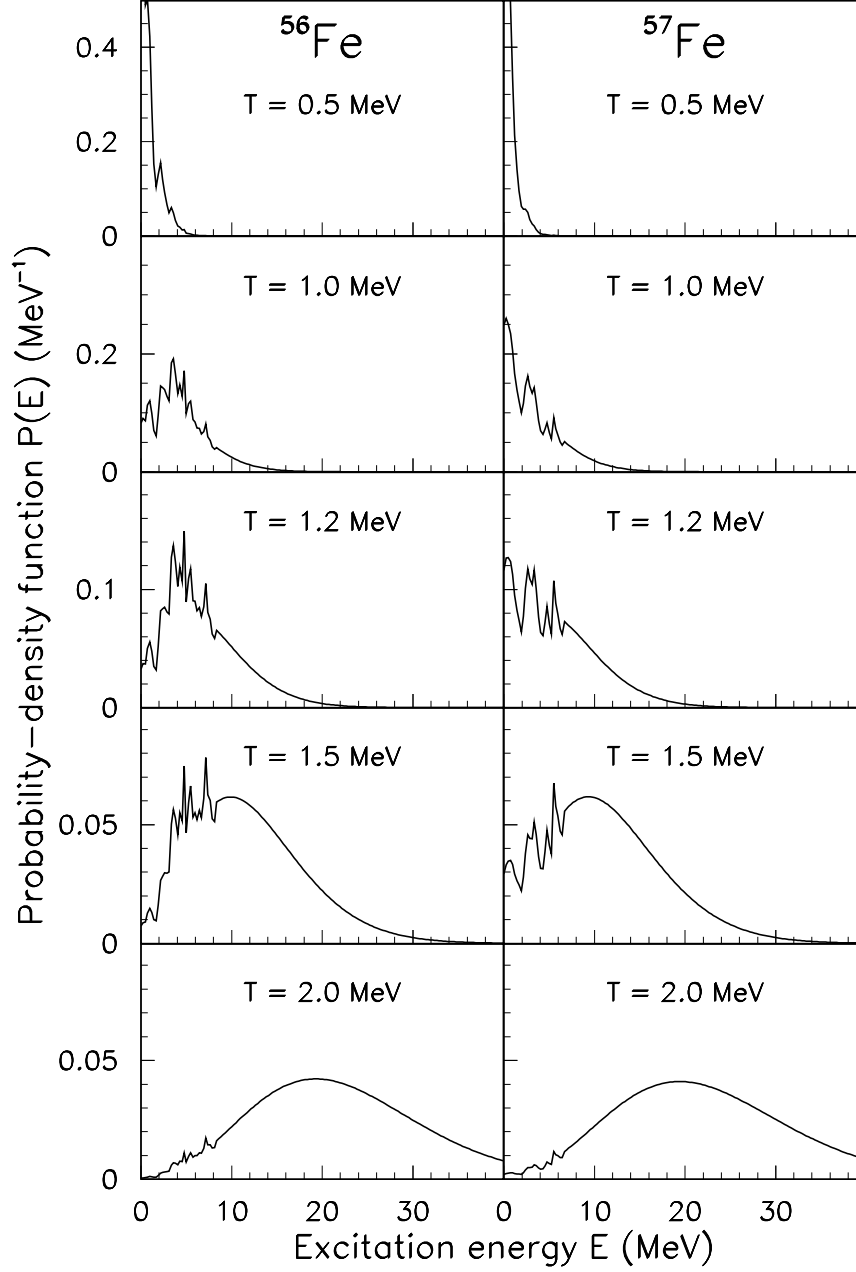


FIG. 6: Observed probability density functions for $^{56,57}\text{Fe}$ for various temperatures.

algorithm that may include a large model space of single-particle states. Since level density is a gross property, the detailed knowledge of the many-particle matrix elements through large diagonalizing algorithms is not necessary.

The single-particle energies e_{sp} are calculated with the Nilsson Hamiltonian for an axially deformed core with a quadrupole deformation parameter ϵ_2 . The spin-orbit and centrifugal

TABLE II: Input parameters for the model calculations.

Isotope	ϵ_2	Δ_π	Δ_ν	A_{rot}	$\hbar\omega_0$	$\hbar\omega_{\text{vib}}$	λ_π	λ_ν
		(MeV)	(MeV)	(MeV)	(MeV)	(MeV)	(MeV)	(MeV)
^{56}Fe	0.24	1.568	1.363	0.120	10.65	2.656	45.89	48.23
^{57}Fe	0.25	1.268	1.465 ^a	0.120	10.72	2.656	45.66	48.40

^a Taken from ^{58}Fe .

parameters κ and μ , together with the oscillator quantum energy $\hbar\omega_0 = 41A^{-1/3}$ MeV between the harmonic oscillator shells, are also input to the code. Within the BCS model, the single-quasiparticle energies are defined by

$$e_{\text{qp}} = \sqrt{(e_{\text{sp}} - \lambda)^2 + \Delta^2}, \quad (15)$$

where the Fermi level λ is adjusted to reproduce the number of particles in the system and Δ is the pair-gap parameter.

In the calculations we have adopted the Nilsson parameters $\kappa = 0.066$ and $\mu = 0.32$ taken from Ref. [30]. The quadrupole deformation ϵ_2 was set to 0.24 for ^{56}Fe , and 0.25 for ^{57}Fe [31]. The Nilsson levels used in the calculations for ^{56}Fe are shown in Fig. 7, with the Fermi levels for the protons and neutrons.

The rotational and vibrational terms, which are schematically added, contribute significantly to the total level density only in the lower excitation region. The rotational parameter A_{rot} was set to 0.12 MeV in order to reproduce the ground-state rotational band of ^{56}Fe [23]. The adopted pairing gap parameters Δ_π and Δ_ν were evaluated from even-odd mass differences [32] according to Ref. [33] (see Table II for a list of all parameters used).

The experimental and calculated level densities for $^{56,57}\text{Fe}$ are shown in Fig. 8. In general, there is a very good overall agreement between the measured level densities and the calculations, even without reducing the pairing gap. This is in contradiction with what is usually thought using the canonical ensemble. However, excitation energy around 8 MeV may be too low to see the overall quenching of the pairing correlations demonstrated in Figs. (4) and (5). Microcanonical and canonical ensembles yield different results for small systems. It is, therefore, no surprise that one measures different thermodynamic quantities within these ensembles.

In Fig. 8, especially for ^{56}Fe , it is gratifying how both the general functional form and the absolute magnitude of the level densities are reproduced. In the case of ^{57}Fe , there is

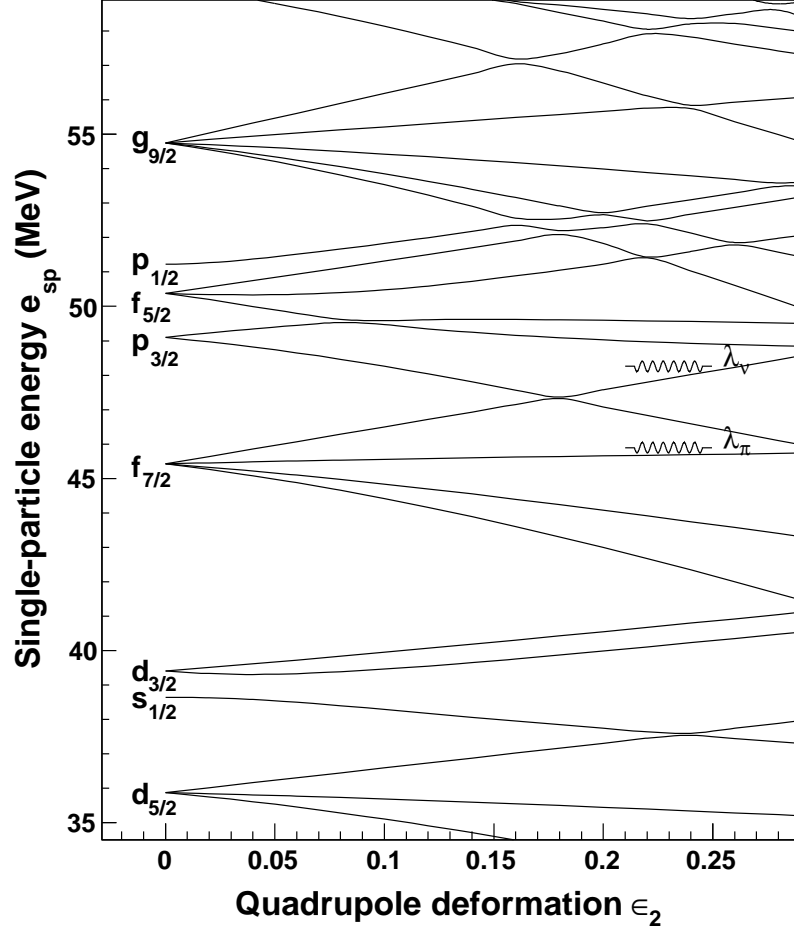


FIG. 7: Nilsson level scheme for ^{56}Fe .

an overshoot in the calculated level density compared to the experimental data from about 3.5 MeV excitation energy. This excess could be due to the neutron $f_{5/2}$, $p_{1/2}$ and $g_{9/2}$ orbitals coming into play too soon, that is, they are too close to the neutron Fermi level. Another possibility is that the adopted (constant) deformation is too large at these excitation energies, where it may be that the nuclear structure favors a more spherical shape.

Figure 9 shows the average number of broken Cooper pairs $\langle N_{\text{qp}} \rangle$ as a function of excitation energy. Both neutron and proton pairs are taken into account, adding up to the total number of broken pairs. From Fig. 9, the pair-breaking process is seen to start at $E \approx 2.5$ MeV for both nuclei, in accordance with the values used for the pair-gap parameters (see Table II).

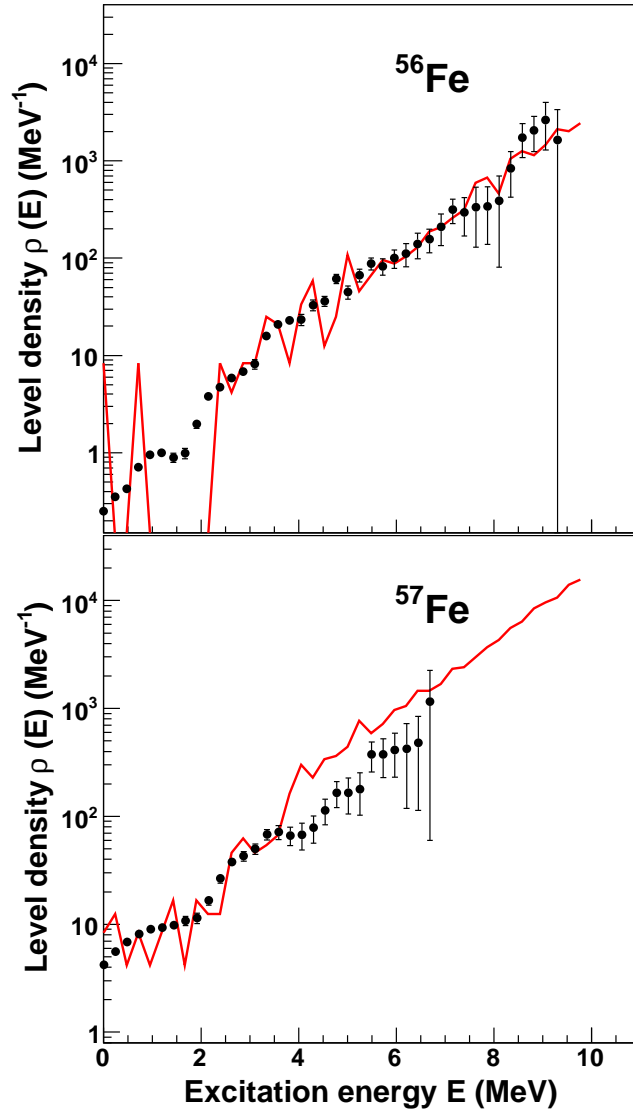


FIG. 8: Calculated level densities (solid line) compared with the experimental ones (data points with error bars) for $^{56,57}\text{Fe}$.

A prominent step structure at $\langle N_{\text{qp}} \rangle = 1$ is seen clearly in ^{56}Fe for excitation energies between $2.5 \leq E \leq 5.5$ MeV, and for ^{57}Fe in the energy region $4.0 \leq E \leq 7.5$ MeV. This means that on average there is one Cooper pair broken, which could be either a proton or a neutron pair. For ^{56}Fe , the total $\langle N_{\text{qp}} \rangle$ exhibits an increase for $E > 5.5$ MeV up to about 9 MeV, where there seems to be a saturation for $\langle N_{\text{qp}} \rangle \approx 2$. This is also reflected in the proton and neutron contributions to $\langle N_{\text{qp}} \rangle$. A similar behavior can be seen in ^{57}Fe for excitation energies higher than ≈ 8 MeV. We observe that the onset of this increase

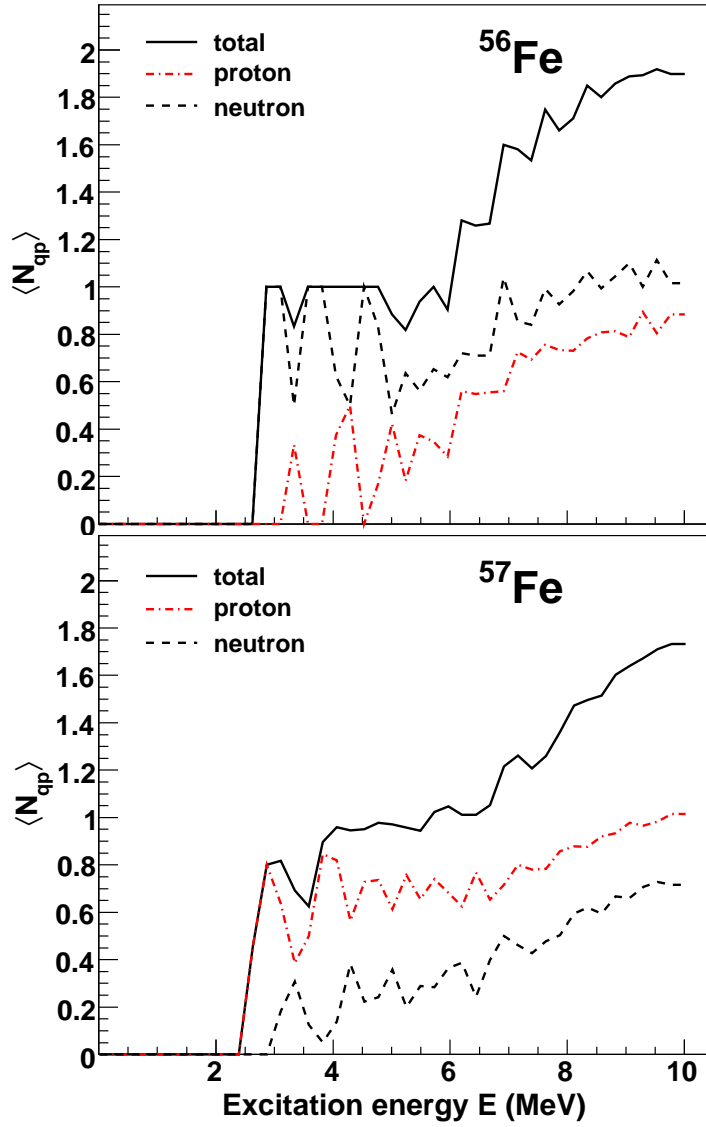


FIG. 9: The average number of broken Cooper pairs as a function of excitation energy for $^{56,57}\text{Fe}$.

is at higher excitation energies than for ^{56}Fe . A possible explanation of this is that the ^{57}Fe valence neutron blocks the quasi-particles created during the pair-breaking process, suppressing the average number of quasi-particles even at high excitation energies. This is supported by the fact that the neutron contribution to the total $\langle N_{qp} \rangle$ is lower or about the same as the proton contribution in ^{57}Fe , while in ^{56}Fe , the neutron contribution is in general higher than the proton contribution.

The present model gives the opportunity of investigating the parity distribution as a function of excitation energy. For this purpose, we utilize the parity asymmetry defined in

Ref. [34] by

$$\alpha = \frac{\rho_+ - \rho_-}{\rho_+ + \rho_-}, \quad (16)$$

which becomes -1 if only negative parity states are present, $+1$ if there are only positive parity states, and 0 when both parities are equally represented. In literature, one also find the expression ρ_-/ρ_+ which relates to α by

$$\frac{\rho_-}{\rho_+} = \frac{1 - \alpha}{1 + \alpha}. \quad (17)$$

The parity asymmetry α for $^{56,57}\text{Fe}$ is shown in Fig. 10.

From Fig. 10, we see that there is an excess of positive parity states in ^{56}Fe and negative parity states in ^{57}Fe . As the excitation energy increases, the parity asymmetry decreases for both nuclei, and shows an almost decay-like behavior, especially in the case of ^{57}Fe . Here, the parity asymmetry is close to zero at $E = 9 - 10$ MeV. For ^{56}Fe , there is still a significant overshoot of positive-parity states in this energy region, giving an average parity asymmetry of $\alpha \approx 0.35$ for $9.5 \simeq E \simeq 10$ MeV.

We have compared our results with the shell-model Monte Carlo results of Y. Alhassid *et al.* [35], and with recent macroscopic-microscopic calculations performed by D. Moele *et al.* [36]. In Fig. 2 of Ref. [36], the ratio ρ_-/ρ_+ is shown for ^{56}Fe , indicating a value of $\rho_-/\rho_+ \simeq 0.1$ at 10 MeV excitation energy. From Fig. 4 in Ref. [35], the ratio $\rho_-/\rho_+ \simeq 0.2$ for $E = 10$ MeV. Using an average parity asymmetry of $\alpha \approx 0.35$ as determined in the previous section, we obtain $\rho_-/\rho_+ \approx 0.5$, which implies a considerable number of additional positive-parity states than predicted by the macroscopic-microscopic model and the shell-model Monte Carlo approach. For ^{57}Fe with $\alpha \approx 0.1$ for $9.5 \simeq E \simeq 10$ MeV, we find $\rho_-/\rho_+ \approx 0.8$. However, one should note that in our calculations, the parity asymmetry strongly depends on the position of the neutron $g_{9/2}$ orbital relative to the Fermi level (see Fig. 7).

V. SUMMARY

Nuclear level densities for $^{56,57}\text{Fe}$ are renormalized using the new level density parameterization suggested by von Egidy and Bucurescu. The level densities obtained with the Oslo method agree well with those obtained from other experiments. The experimental level densities are used to extract thermodynamic quantities. The entropies for $^{56,57}\text{Fe}$ obtained in the

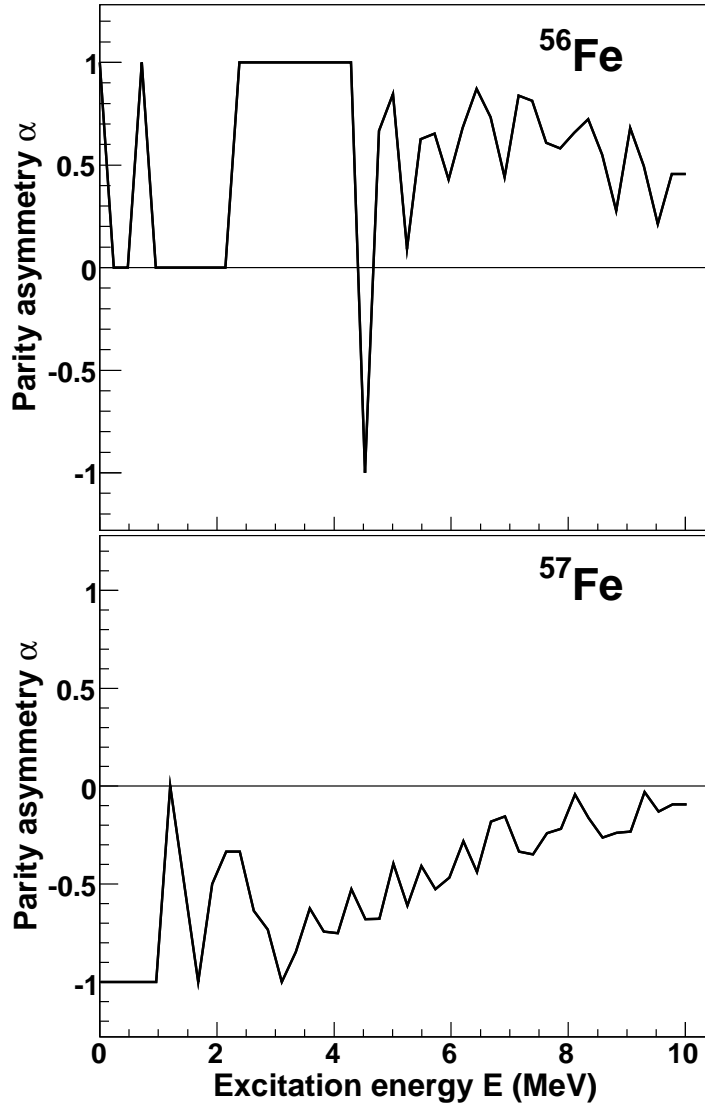


FIG. 10: The parity asymmetry as function of excitation energy for $^{56,57}\text{Fe}$.

microcanonical ensemble reveal step structures indicating the breaking of nucleon Cooper pairs. The entropy carried by the single neutron at higher excitation energies ($4 \text{ MeV} < E < 7 \text{ MeV}$) is estimated to be $\Delta S = 1.2(4)k_B$ which is smaller than that of the rare-earth isotopes.

Assuming a constant ΔS , a critical temperature for the depairing process was determined. In the canonical ensemble, several thermodynamic properties were investigated. Probability density functions for $^{56,57}\text{Fe}$ were also extracted which reveal the difference between small systems such as the atomic nucleus and a system in the thermodynamic limit.

Microscopic model calculations based on BCS quasiparticles were performed. The overall agreement between the experimental and calculated level densities are good. Step structures observed in the experimental level densities are also observed in the plot of the average number of broken pairs as a function of excitation energy. The parity distributions obtained from model calculations for $^{56,57}\text{Fe}$ indicate a decrease of parity asymmetry for both isotopes as the excitation energy increases. The microscopic model, which is expressed within the microcanonical ensemble (fixed E with no heat bath), describes the observed level densities without the need of attenuation of the pairing-gap energies for excitation energies below 8 MeV.

Acknowledgments

This work was supported in part by the U.S. Department of Energy under grants number DE-FG02-97-ER41042 and DE-FG52-06NA26194. In addition, this work was performed under the auspices of the U.S. Department of Energy by the University of California, Lawrence Livermore National Laboratory under contract No. W-7405-ENG-48. Financial support from the Norwegian Research Council (NFR) is gratefully acknowledged.

-
- [1] D. Kusnezov, Y. Alhassid, and K. A. Snover, Phys. Rev. Lett. **81**, 542 (1998).
 - [2] M. D'Agostino *et al.*, Phys. Lett. B **371**, 175 (1996).
 - [3] P. Chomaz, V. Duflot, and F. Gulminelli, Phys. Rev. Lett. **85**, 3587 (2000).
 - [4] M. Sano and S. Yamasaki, Prog. Theor. Phys. **29**, 397 (1963).
 - [5] T. Sumaryada and A. Volya, Phys. Rev. C **76**, 024319 (2007).
 - [6] A. Schiller, M. Guttormsen, M. Hjorth-Jensen, J. Rekstad, and S. Siem, Phys. Rev. C **66**, 024322 (2002).
 - [7] K. Kaneko and A. Schiller, Phys. Rev. C **75**, 044304 (2007).
 - [8] B. K. Agrawal, T. Sil, S. K. Samaddar, and J. N. De, Phys. Rev. C **63**, 024002 (2001).
 - [9] J. L. Egido, L. M. Robledo, and V. Martin, Phys. Rev. Lett. **85**, 26 (2000).
 - [10] S. Liu and Y. Alhassid, Phys. Rev. Lett. **87**, 22501 (2001).
 - [11] A. Schiller, A. Bjerje, M. Guttormsen, M. Hjorth-Jensen, F. Ingelbretsen, E. Melby, S. Messelt,

- J. Rekstad, S. Siem, and S. W. Ødegård, Phys. Rev. C **63**, 021306(R) (2001).
- [12] M. Guttormsen, T. S. Tveter, L. Bergholt, F. Ingebretsen, and J. Rekstad, Nucl. Instrum. Methods Phys. Res. A **374**, 371 (1996).
 - [13] M. Guttormsen, T. Ramsøy, and J. Rekstad, Nucl. Instrum. Methods Phys. Res. A **255**, 518 (1987).
 - [14] D. M. Brink, Ph.D. Thesis, Oxford University (1955).
 - [15] P. Axel, Phys. Rev. **126**, 671 (1962).
 - [16] A. Schiller, L. Bergholt, M. Guttormsen, E. Melby, J. Rekstad, and S. Siem, Nucl. Instrum. Methods Phys. Res. A **447**, 498 (2000).
 - [17] A. Voinov, M. Guttormsen, E. Melby, J. Rekstad, A. Schiller, and S. Siem, Phys. Rev. C **63**, 044313 (2001).
 - [18] S. F. Mughabghab, *Atlas of Neutron Resonances*, 5th ed. (Elsevier Science 2006).
 - [19] T. von Egidy and D. Bucurescu, Phys. Rev. C **72**, 044311 (2005), and Phys. Rev. C **73**, 049901 (E).
 - [20] A. Voinov *et al.*, Phys. Rev. C **74**, 014314 (2006).
 - [21] A.V. Voinov, S. M. Grimes, C. R. Brune, M. J. Hornish, T. N. Massey, and A. Salas, Phys. Rev. C **76**, 044602 (2007).
 - [22] A. Voinov, E. Algin, U. Agvaanluvsan, T. Belgia, R. Chankova, M. Guttormsen, G. E. Mitchell, J. Rekstad, A. Schiller, and S. Siem, Phys. Rev. Lett. **93**, 142504 (2004).
 - [23] R. Firestone and V. S. Shirley, *Table of Isotopes*, 8th ed. (Wiley, New York, 1996), Vol. II.
 - [24] A. Schiller, U. Agvaanluvsan, E. Algin, A. Bagheri, R. Chankova, M. Guttormsen, M. Hjorth-Jensen, J. Rekstad, S. Siem, A.C. Sunde, and A. Voinov, AIP Conf. Proc. 777, 216 (2005).
 - [25] E. Tavukcu, Ph.D. thesis, North Carolina State University (2002).
 - [26] M. Guttormsen, M. Hjorth-Jensen, E. Melby, J. Rekstad, A. Schiller, and S. Siem, Phys. Rev. C **63**, 044301 (2001).
 - [27] M. Guttormsen, M. Hjorth-Jensen, E. Melby, J. Rekstad, A. Schiller, and S. Siem, Phys. Rev. C **64**, 034319 (2001).
 - [28] A. C. Larsen, M. Guttormsen, R. Chankova, F. Ingebretsen, T. Lönnroth, S. Messelt, J. Rekstad, A. Schiller, S. Siem, N. U. H. Syed, and A. Voinov, Phys. Rev. C **76**, 044303 (2007).
 - [29] J. Bardeen, L. N. Cooper, and J. R. Schrieffer, Phys. Rev. **108**, 1175 (1957).
 - [30] D. C. S. White, W. J. McDonald, D. A. Hutcheon, and G. C. Neilson, Nucl. Phys. **A260**, 189

- (1976).
- [31] RIPL-1: Handbook for calculations of nuclear reaction data, IAEA, Vienna, Report No. IAEA-TECDOC-1024 (1998); RIPL-2: Handbook for calculations of nuclear reaction data, IAEA, Vienna, Report No. IAEA-TECDOC-1506 (2006).
URL: <http://www-nds.iaea.org/RIPL-2/>
 - [32] G. Audi and A.H. Wapstra, Nucl. Phys. **A595**, 409 (1995).
 - [33] A. Bohr and B. Mottelson, *Nuclear Structure*, (Benjamin, New York, 1969), Vol. I, p. 169.
 - [34] U. Agvaanluvsan, G. E. Mitchell, J. F. Shriner Jr., and M. Pato, Phys. Rev. C **67**, 064608 (2003).
 - [35] Y. Alhassid, G. F. Bertsch, S. Liu, and H. Nakada, Phys. Rev. Lett. **84**, 4313 (2000).
 - [36] D. Mocerlj, T. Rauscher, G. Martínez-Pinedo, K. Langanke, L. Pacearescu, A. Faessler, F.-K. Thielemann, and Y. Alhassid, Phys. Rev. C **75**, 045805 (2007).